⌘ *Author's Choice*

THE JOURNAL OF BIOLOGICAL CHEMISTRY VOL. 287, NO. 18, pp. 14950–14959, April 27, 2012
Published in the U.S.A.

Cross-seeding and Conformational Selection between Three- and Four-repeat Human Tau Proteins*[S]

Received for publication, January 8, 2012, and in revised form, February 21, 2012 Published, JBC Papers in Press, March 5, 2012, DOI 10.1074/jbc.M112.340794

Xiang Yu[‡], Yin Luo[‡§], Paul Dinkel[¶], Jie Zheng[‡1], Guanghong Wei[§2], Martin Margittai[¶], Ruth Nussinov[‖3], and Buyong Ma[‖]**

*From the [‡]Department of Chemical & Biomolecular Engineering, The University of Akron, Akron, Ohio 44325, the [§]State Key Laboratory of Surface Physics, the Key Laboratory for Computational Physical Sciences (Ministry of Education), and the Department of Physics, Fudan University, Shanghai, China, the [¶]Department of Chemistry & Biochemistry, University of Denver, Denver, Colorado 80208, the [‖]Basic Research Program, SAIC-Frederick, Inc. Center for Cancer Research Nanobiology Program, NCI-Frederick, Frederick, Maryland 21702, and the **Department of Human Genetics and Molecular Medicine, Sackler Institute of Molecular Medicine, Sackler School of Medicine, Tel Aviv University, Tel Aviv 69978, Israel*

Background: K18/K19 Tau protein isoforms can aggregate into different amyloid-β-like fibrils.
Results: Different K18/K19 oligomers can be templates for fibril growth via cross-seeding between K18 and K19.
Conclusion: K18 and K19 octamers create different cross-seeding barriers promoting K18 growth on K19 seeds but preventing K19 growth on K18.
Significance: Conformational selection of compatible states during cross-seeding of amyloid species is general in amyloid-related diseases.

In Alzheimer's disease and frontotemporal dementias, the microtubule-associated protein Tau forms intracellular paired helical filaments. The filaments can form not only by the full-length human Tau protein, but also by the three repeated (K19) or four repeated (K18) Tau segments. However, of interest, experimentally, K19 can seed K18, but not vice versa. To obtain insight into the cross-seeding between K18 and K19 aggregates, here, K18 and K19 octamers with repeat 3 (R3) in U-shaped, L-shaped, and long straight line-shaped (SL-shape) conformations are assembled into different structures. The simulation results show that K18-8/K19-8 (K18 and K19 assemblies number 8) with R3 in an L shape and K18-9/K19-9 with R3 in an SL shape are highly populated and present the highest structural similarity among all simulated K18 and K19 octamers, suggesting that similar folding of K18/K19 may serve as structural core for the K18-K19 co-assembled heterogeneous filament. We demonstrate that formation of stable R2 and R3 conformations is the critical step for K18 aggregation, and R3 is critical for K19 fibrillization. The different core units in K18 and K19 may create a cross-seeding barrier for the K18 seed to trigger K19 fibril growth because R2 is not available for K19. Our study provides insights into cross-seeding involving heterogeneous structures. The polymorphic nature of protein aggregation could be magnified in the cross-seeding process. If the seeding conformations lead to too much divergence in the energy landscape, it could impede fibril formation. Such an effect could also contribute to the asymmetric barrier between K18 and K19.

The significant pathological symptom of Alzheimer's disease is often characterized by the coexistence of two different amyloid deposits in the patient's brain. The extracellular senile plaques are composed of amyloid-β (Aβ)[4] fibrils, whereas the intracellular tangles are composed of paired helical filaments of the microtubule-associated protein Tau (1, 2). The physiological function of Tau is to bind and stabilize microtubules in the axons of the neurons; hence the expression of Tau protein is strongly up-regulated during neuronal development (3). However, inappropriate folding of Tau protein will lead to the formation of paired helical filaments or straight filaments. Tau protein ranging in size from 352 to 441 amino acids can be divided into two major groups. The first group is 4R Tau (hTau40, hTau34, hTau24, and K18) with four microtubule binding repeats (R1, R2, R3, and R4), and the second group is 3R Tau (hTau39, hTau37, hTau23, and K19) with three microtubule binding repeats (R1, R3, and R4) (4). 3R and 4R Tau proteins are produced in adult human brains at equimolar ratios (5), and both groups are found in Alzheimer's brain (6).

Similar to Aβ monomers in bulk solution, small angle x-ray scattering, CD, and infrared spectroscopy have demonstrated that the isolated Tau protein in solution is in a random coil conformation (7, 8). Although mechanistic studies of Tau pro-

* This work was supported, in whole or in part, by National Institutes of Health Grant R01NS076619 (to M. M.). This work was also supported by National Cancer Institute Contract HHSN261200800001E, the intramural research program of the National Cancer Institute Center for Cancer Research, National Science Foundation CAREER Award CBET-0952624 (to J. Z.), a 3M nontenured faculty award (to J. Z.), National Natural Science Foundation of China Grant 11074047 (to G. W.), and Research Fund for the Doctoral Program of Higher Education of China Grant RFDP-20100071110006 (to G. W.).
⌘ *Author's Choice*—Final version full access.
[S] This article contains supplemental Table S1 and Figs. S1–S5.
[1] To whom correspondence may be addressed. Tel.: 330-972-2096; Fax: 330-972-5856; E-mail: zhengj@uakron.edu.
[2] To whom correspondence may be addressed. Tel.: 86-21-55665231; Fax: 86-21-65104949; E-mail: ghwei@fudan.edu.cn.
[3] To whom correspondence may be addressed. Tel.: 301-846-5579; Fax: 301-846-5598; E-mail: ruthnu@helix.nih.gov.

[4] The abbreviations used are: Aβ, amyloid-β; RMSD, root mean square derivation; SL, long straight line; MD, molecular dynamics; GBMV, generalized Born method with molecular volume; HB, hydrogen bond; SC, side chain contact; RMSF, root mean square fluctuation; AFM, atomic force microscopy.

tein aggregation and the subsequent filament formation *in vitro* have also revealed certain kinetic similarities to Aβ aggregation such as the formation of cross-β structure (9, 10), nucleation-dependent mechanism (11), and on or off pathway intermediates (12), the structural features and driving forces that control Tau aggregation are still unclear. The formation of fibrillar Tau structure usually requires the addition of nucleating polyanionic co-factors such as (heparin), which suggests the important role of electrostatic interaction in inducing the appropriate conformation for aggregation. Continuing efforts have gradually revealed parts of the inner structure of Tau fibrils. It has been reported that the microtubule-binding domains (R1, R2, R3, and R4) first become structured and form a protease-resistant core of full-length Tau aggregates (13–15). Among these four repeats are the R2 and R3 repeats, which contain two critical hexapeptides (^{275}VQIINK^{280} and ^{306}VQIVYK^{311}) for Tau aggregation buried deeply inside of the filament structure (16) and have a high propensity to form parallel in-register β-structure (17–19). This highlights the importance of R2 and R3 as the structural core for Tau fibrillar structures. Recently, experiments co-assembling and cross-seeding the 3R/4R Tau protein confirmed the existence of a common core structure for both 3R and 4R Tau filaments (4, 20). Apart from this structural information, atomic data relating to the Tau fibrillar structure with different sizes, association interfaces, and symmetries along the lateral direction are not available to date, which has prevented further exploration of the aggregation and cross-assembling mechanisms of 3R/4R Tau proteins.

Mutual conformational selection and population shift are the key mechanism in biomolecular recognition (21–23), and monomers and small oligomers binding to amyloid seeds in fibril growth is a molecular recognition event (24). Cross-seeding of amyloid species is governed by conformational selection of compatible (complementary) states. If the dominant conformations of two species are similar, they can cross-seed each other; on the other hand, if they are sufficiently different, they will grow into different fibrils, reflecting species barriers. Such a scenario has recently been observed for the Tau protein. The constructs of K18 and K19 are N/C termini-cleaved 4R and 3R Tau proteins. Their aggregates show structural features that are consistent with those of the full-length Tau protein (4, 20). Therefore, K18/K19 is viewed as simplified 4R/3R Tau proteins. Although a construct consisting of R1, R3, and R4 can serve as a seed for the entire R1, R2, R3, and R4 Tau segments, the inverse does not hold (4).

Tau filaments could play an important role in the propagation of the aggregation from one cell to the others (25), and filaments can be transferred among neighboring cells in tissue culture (26). It has been also observed that injection of insoluble Tau protein into mouse brain resulted in the spreading of misfolding through different brain regions (27). Thus, the investigation of K18 and K19 peptide folding and aggregation is not only able to provide useful insight into 4R and 3R Tau fibrillar structure and aggregation mechanisms but can also provide general insights into amyloid formation with prion-like transmission.

To understand the detailed conformational selection mechanisms involved in the fibril formation of K18 and K19, we extensively probe the potential structures and related populations of fibril-like oligomers of K18 and K19. By analyzing the structural and energetic contributions, we found that different repeats contribute differentially to the structural stabilities of the K18 and K19 oligomers. The combination of the various arrangements of the repeats leads to the highly polymorphic nature of K18 and K19 fibril-like oligomers, many of which are potential templates for fibril growth via cross-seeding action between K18 and K19. Finally, we provide insight into the conformational selection involved in K18 and K19 fibril formations, which underlies the asymmetric barriers between K18 and K19 cross-seeding.

MATERIALS AND METHODS

Construction of K18/K19 Octamers—Based on experimental fibril dimension and previous theoretical studies, we constructed three classes with a total of eighteen K18/K19 octamers with the conformation of R3 varying from a U shape, to an L shape, to a straight line (SL) shape with the goal of examining the stability of K18 and K19 octamer conformations. The sizes of K18 and K19 fibrils have been carefully characterized by AFM, showing that the heights of K18 and K19 fibrils are ~8.0–8.8 and 6.9–10.2 nm, respectively (15). Recently, using molecular dynamics (MD) simulations, Miller *et al.* (28) confirmed that R2, R3, and R4 Tau repeats can adopt a U-shaped conformation. Simulation data suggest that U-shaped repeats can serve as stable building blocks (29, 30) for K18/K19 fibril polymorphism. However, considering the polymorphic nature of amyloid oligomers and fibrils (31–33), it is very likely that R2, R3, and R4 repeats adopt different conformations that facilitate Tau aggregation. We first built U-shape R1, R2, R3, and R4 octamers (supplemental Fig. S1) as previously described (28) and then connected them with PGGG flexible region to construct six K18 (K18-1, -2, -3, -4, -5, and -6) and five K19 (K19-1, -2, -3, -6, and -7) octamers (see Fig. 1 and supplemental Fig. S1) with R3 in a U shape. The detailed procedures to construct K18 models were shown in supplemental Fig. S2. The same procedures were applied to construct K19 models. K18-1, K18-2, K18-3, K18-5, and K18-6 are five models with all four repeats in a U shape. Each of these five octamers displayed distinct morphologies based on different organizations among R1, R2, R3, and R4 repeats. In K18-1, repeats R2, R3, and R4 were arranged in parallel with R1 covering the PGGG connecting domains of R2-R3 and R3-R4. K18-2 was a model with R1, R2, and R3 aligned in parallel on top of each other, whereas the whole R4 associated with R1/R2/R3 sidewise and was the only repeat exposed to bulk solution. Similar to K18-2, R4 in K18-3 also exposed in bulk solution but with its N-terminal strands covering the PGGG connecting domains of R2-R3 and R3-R4. K18-4 was the only model with R2 in an L shape. This model allows examination of the conformational effect of R2 on K18 octamer structural stability. K18-5 was a simple model with all four repeats arranged in parallel. K18-6 was a model with R1, R2, and R3 arranged in parallel and R2 exposed to bulk solution connected with R1 and R3 by PGGG domains. The construction of K19-1, K19-2, K19-3, K19-6, and K19-7 models was similar to K18-1, K18-2, K18-3, K18-6, and K18-5, except for the absence of R2 repeat in all K19 octamers. Because only one paired helical

filament segment, ^{306}VQIVYK^{311}, is preserved in K19 Tau isoforms, we also tested K19 models with R3 in an L shape and R3 in a SL shape to fully examine the possibility of polymorphism of the R3 repeat. The conformations of R1, R2, and R4 were also adjusted to achieve the maximal contacts with the R3 repeat. For the L-shaped K18 and K19 octamers, the U turn region ^{315}LLKVT^{319} of R3 was opened, with U-shaped R1/R2 and R4 covering the two sides of the long R3 strands (K18-7 and K19-7). To examine the effect of the conformational change of R4 on the structural stability of K18 and K19 octamers with R3 in an L shape, we also extended R4 into a long L shape, which cooperates with R1/R2 to fully wrap the R3 repeat (K18-8 and K19-8). For K18 and K19 models with R3 in SL shape, not only R3 repeat, but also other repeats were rearranged into straight β-strands to achieve the maximal residue interactions between two neighboring repeats and structural rigidity.

Overall, all K18 and K19 octamers were constructed with interpeptide distances of 4.7 Å, and the specific peptide residue arrangements are described in supplemental Fig. S1. The interface of two neighboring repeats and the arrangement of charged residues (both charged surface exposure and salt bridge formation) were optimized by slightly changing the coordinates of residues in each model.

Explicit Solvent MD Simulation Protocol—All of the MD simulations were performed by the NAMD (34) program using the Charmm27 force field, including dihedral cross-term correction dihedral cross-term energy correction map (35) for peptides and modified transferable intermolecular potential functions for three points (TIP3P) water molecules. The Tau oligomers were energy-minimized and explicitly solvated in a TIP3P water box with a minimum distance of 15 Å from any edge of the box to any Tau atom. Any water molecule within 2.5 Å of Tau was removed. Counterions of NaCl were added to neutralize the systems.

The solvated and ionized system was subject to energy minimization for 4000 steepest decent steps. The energy-minimized system was then gradually heated up to 310 K and equilibrated for 600 ps with the backbone positions constrained, followed by additional equilibrium with hydrogen bond distance between the β-strands of Tau proteins fixed in the range of 1.8–2.5 Å for 1 ns before the 40-ns MD production run. These conditions were applied to all models in our study. Both equilibrium and production runs were performed using a constant number of molecules, pressure, and temperature ensemble under periodic boundary conditions. Constant pressure (1 atm) and temperature (310 K) were maintained by an isotropic Langevin barostat with a decay period of 100 fs and a Langevin thermostat with a damping coefficient of 5 ps^{-1}. The simulation temperature of 310 K is consistent with human body temperature to better mimic the real Tau protein folding environment.

The long range electrostatic interactions were treated by the particle mesh Ewald method using a real space cutoff of 12 Å and a gird size of ~ 1 Å in all directions. The short range van der Waals interactions were calculated using a switching function with a twin range cutoff of 10 and 12 Å. The velocity Verlet integrator with a time step of 2 fs was used to solve Newton's equation of motion. Any bond involving hydrogen atoms were constrained by the RATTLE algorithm. Nonbonded and image lists were updated every 20 integrator with a time step of 20 integration steps.

Structural Population Analysis—To evaluate the relative structural population of Tau oligomers, the Tau protein trajectory for each system was extracted from the last 5 ns of explicit solvent MD with water molecules and ions excluded. The conformation energies of all systems were calculated using the generalized Born method with molecular volume (GBMV) (36) after 700 steps of energy minimization to relax the local geometries caused by the thermal fluctuations which occurred in the MD simulations. A total of 11,250 conformations (1250 conformations for each of the nine conformers examined) were used to construct the effective energy landscape of K18 and K19 octamers and to evaluate the conformer probabilities by using an in-house Monte Carlo program (37). Briefly, for any two randomly selected conformers of *i* and *j*, the Boltzmann factor was computed by $e^{-(Ej-Ei)/KT}$, where E_i and E_j are the conformational energies obtained from the GBMV calculations for conformation *i* and *j*, respectively; *K* is the Boltzmann constant; and *T* is the absolute temperature (310 K is the temperature for MD simulation). If the Boltzmann factor value is larger than the random number, the structural transition from conformation *i* to conformation *j* is accepted. Throughout one million steps, the number of conformations visited by each conformer was counted. Finally, the relative probability of each conformer was evaluated as $P_n = N_n/N_{total}$. It should be noted that the populations of the conformers are only indicative, and they are sensitive to the conformation energy for each conformer.

Protein Expression and Purification—K18 and K19 (cysteines substituted by serines) were expressed and purified as previously described utilizing their heat stability and elevated isoelectric points (4, 20). Purified proteins were precipitated and stored at −80 °C. For further use, protein pellets (4–6 mg) were taken up in 8 M guanidine hydrochloride. The denaturant was exchanged with reaction buffer (100 mM NaCl, 10 mM Hepes, pH 7.4) by passing the samples over PD-10 desalting columns (GE Healthcare). Protein concentrations were determined by the BCA method (Pierce).

Seeded Filament Growth and Sedimentation—25 μM of K18 and K19 were mixed with 50 μM heparin (average molecular mass of 5,000 Da; Celsus, Cincinnati, OH) and allowed to form filaments under agitation for 3 days at 25 °C. Subsequent sonification of the filaments (500 μl) for 20 s at power setting 3 in a Fisher Scientific Sonifier (150 series) resulted in Tau seeds with an average length of 200 nm (as judged by transmission electron microscopy). 3 mol % K18- or K19 seeds were added to 10 μM monomeric K19 in reaction buffer containing 20 μM heparin. The samples were incubated quiescently for 3 h at 37 °C. (The presence of 2 mol % acrylodan-labeled Tau (linked to a cysteine in position 310) allowed monitoring of filament growth by fluorescence spectroscopy (4). After the completion of filament growth, protein aggregates were sedimented for 40 min at 100,000 × *g*. The pellets were taken up in equal volumes of gel loading buffer and applied onto a 15% SDS-PAGE gel. The proteins were stained with Coomassie Blue and quantified by densitometry.

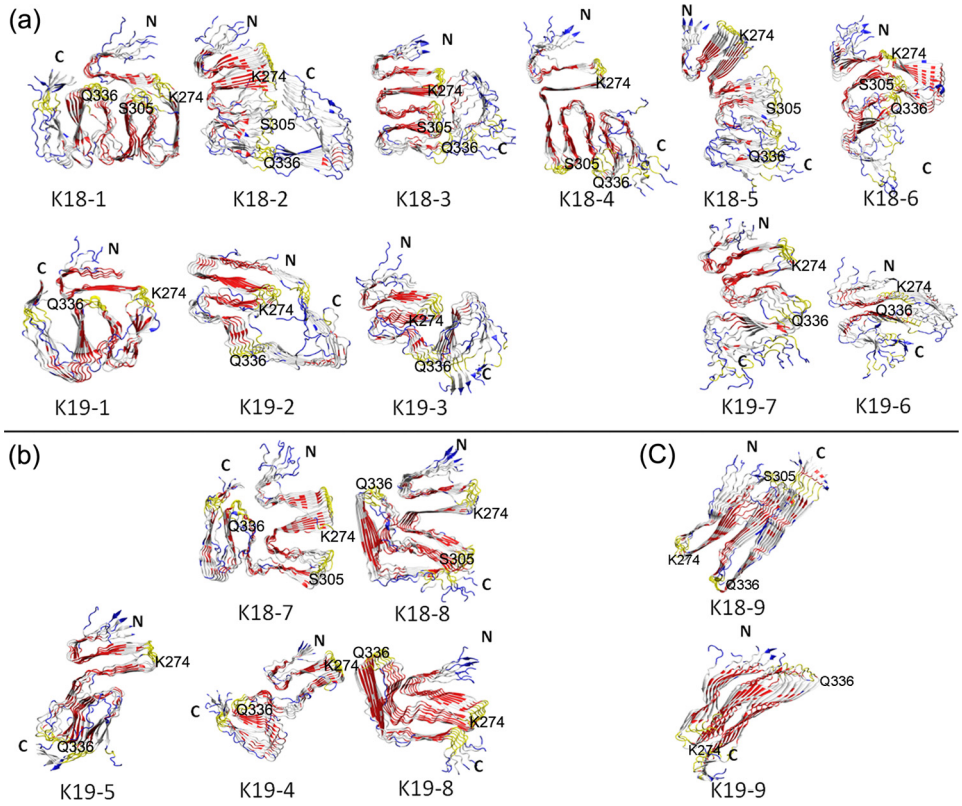

FIGURE 1. **Atomic structures of K18 octamers consisting of R1, R2, R3, and R4 repeats and the corresponding K19 octamers consisting of R1, R3, and R4 repeats, averaged from the last 5-ns MD simulations.** Based on the conformation of R3 repeats, K18 and K19 octamers are divided into three groups: U-K18/K19 (*a*), L-K18/K19 (*b*), and SL-K18/K19 (*c*) octamers. The residue-based RMSF is imposed on each averaged structure to reflect local structural flexibility, using a blue-white-red scale with low RMSF of <3 Å (*red*), moderate RMSF of 3–6 Å (*white*), and high RMSF >6 Å (*blue*). The β-sheet regions display the lower RMSF, whereas the turn and tail regions exhibit the higher RMSF.

RESULTS

K18 and K19 Octamers Display Different Structure Stabilities but Share Some Common Features—Backbone root mean square derivation (RMSD) calculation suggests that all K18 and K19 octamers experienced initial fast structural relaxation and swelling at the first 5 ns and then stabilized at an equilibrium state after 30 ns. Moderate structural adjustment was observed for K18/K19 octamers by comparing initial structures (supplemental Fig. S1) with final structures averaged from the last 5 ns (Fig. 1). Most K18 and K19 octamers were able to maintain their structural integrity with highly conserved hydrogen bonds (>83.9%) and side chain contacts (>90.7%) during 40-ns MD simulations (supplemental Table S1). Examination of the MD trajectories of both K18 and K19 octamers showed that large structural fluctuation occurred mostly at the U-turn region and the PGGG region because of the flexible nature of these structural motifs and sequences, resulting in some structural transition from the initial β-structures to random structures near the N-terminal strand of R1 repeat for all of K18 and K19 octamers.

Among K18 octamers, the L-K18 octamers (K18-3, K18-4, K18-7, and K18-8) and the SL-K18 octamer (K18-9) generally had better structural integrity than U-K18 octamers (K18-1, K18-2, K18-5, and K18-6), as evidenced by smaller backbone RMSD (<6.5 Å for L-K18 and SL-K18 and >7.0 Å for U-K18) and more well preserved hydrogen bonds (HBs) and side chain contacts (SCs) (>91.7% HB and 94.1% SC for L/SL-K18, and >85.8% HB and 91.6% SC for U-K18). Among the U-K18 octamers, K18-2 and K18-5, whose R1, R2, and R3 repeats are packed on top of each other, showed the least structural stability because of the loss of 50% of HBs and 80% of SCs. In K18-2, the R4 marginally contacted with R1/R2/R3 repeats via salt bridges between Lys^{274} at the end of R1 and Glu^{372} at the end of R4. Because the R4 was completely exposed to the bulk solution, such salt bridges were insufficient to maintain the association of R4 with other repeats. In K18-5, R4 repeats were aligned in parallel to R3. The limited interaction between N-terminal strands and C-terminal strands of R2 did not compensate for the tension in the R2 U-turn. Therefore, within 40 ns of MD simulations, the N- and C-terminal strands of R2 tended to dissociate from each other. The structural dynamics of R2 in K18-5 suggests that the external force is necessary to constrain R2 in the U-shaped conformation. This was confirmed by the K18-1 and K18-3 structures. The PGGG region of R2 contacting with R1 in K18-1 or R4 in K18-3 was well maintained with backbone RMSD of ~4 Å for R2 repeats. K18-4 is the only model with R2 in an L shape, which makes the inner side of R2 contact with R3. Although K18-4 experienced large structural adjustment with a backbone RMSD of 9.9 Å, which mainly originated from R1 and R3 repeats, L-shaped K18-4 preserved more HBs and SCs than other U-K18 octamers. The L-K18 octamers (including K18-7 and K18-8) and the SL-K18 octamer (K18-9) exhibited limited structural derivations with backbone RMSDs of ~6.5 Å. The smaller RMSDs and the higher HBs/SCs suggest that L-K18 and SL-K18 octamers can

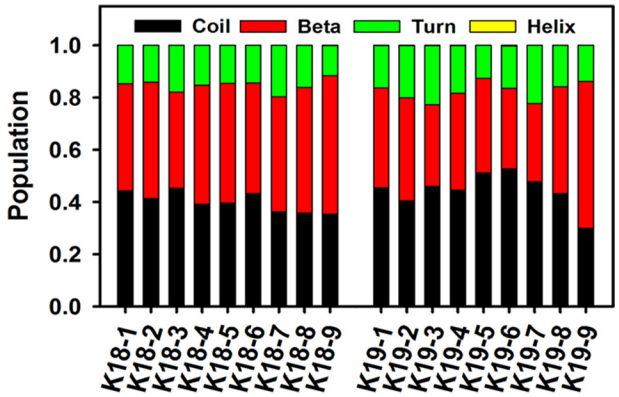

FIGURE 2. **Secondary structure populations of K18 and K19 octomers calculated by the STRIDE method.** β-Structure (*red bar*) and random coil (*black bar*) are dominant secondary structures, whereas turn (*green bar*) is a minor but non-negligible conformation.

better maintain their initial conformations than U-K18 octamers.

All K19 octamers without R2 repeats adopted conformations similar to the corresponding K18 octamers with R2 repeats. However, most K19 octamers (except for K19-6 and K19-7) experienced smaller structural deviations (~1 Å) than the corresponding K18 octamers. The exclusion of R2 from K19 oligomers also led to better β-sheet structure preservation in R4 (22.4% averaged over all K19 oligomers) than the K18 oligomers (13.65% averaged over all of K18 oligomers). Comparison of U-K19 octamers with L/SL-K19 octamers revealed that U-K19 octamers had larger backbone RMSDs than L-K19 and SL-L19 octamers and comparable RMSDs to U-K18 octamers. Consistent with K18-5 and K18-6 octamers that had the largest backbone RMSDs among K18 octamers, K19-7 showed the largest backbone RMSD of 13.3 Å. For those K18 and K19 models with R1, R2, R3, and R4 or R1, R3, and R4 parallel stacking together, they often experienced large structural rearrangement, suggesting that this packing of the repeats is not a favorable conformation for Tau fibrillar structure. K19-3 is another U-K19 octamer with a low HB/SC preservation ratio. Examination of the MD trajectory showed that R4 repeats gradually disassociated from the PGGG region in R1. Compared with K18-3 that had two PGGG regions in contact with R4 repeats, the interactions between the single PGGG region in R1 and R4 repeats in K19-3 were not sufficient to associate the isolated R4 with other repeats. Without R2 repeats in the L-K19 and SL-K19 octamers, they had much smaller backbone RMSDs than the corresponding K18 octamers. K18-8/K19-8 had the smallest RMSD and the highest HBs, whereas K18-9/K19-9 had the largest HB/SC preservation ratio. This suggests that R3 and R4 in extended conformation (L or SL shape) may form a more compact and stable core structure that facilitates Tau protein fibrillization.

β-Structure Locates at Specific Regions in K18 and K19 Octamers—Although the Tau monomer does not adopt a dominant secondary structure, cross-β structure exists in the core of the Tau fibril (10, 19, 38). Secondary structure populations for all K18 and K19 octamers over the last 5 ns were averaged by the STRIDE algorithm (39). Fig. 2 showed that as compared with over 70% of the β-structures in mature Aβ fibrils (40, 41), all of the K18 and K19 octamers with U-shaped or L-shaped repeats only contained ~28–43% of β-structures. Only SL-shaped K18-9 and K19-9 with straight repeats maintained 53.0% and 56.3% β-structures, respectively. A plausible reason for the difficulty of U- and L-shaped K18 and K19 octamers to form β-structure is that the highly concentrated and positively charged residues exert strong repulsive forces. These forces are overcome by polyanions (such as heparin), which accelerate aggregation. Similar to the polymorphic nature of Aβ oligomers, protofibrils, and fibrils, highly ordered Tau octamers exhibited heterogeneous and dynamic structures with a wider variety of secondary structural populations of partially folded coils (38.7–52.7%), β-structures (28.5–56.3%), and turns (16.2–22.8%). However, it is not necessary for K18/K19 and full-length Tau filaments to largely adopt well defined β-structures to form the final Tau fibrils. For example, K18-3 and K18-4 octamers are likely to serve as core structures for mature Tau fibril growth.

It is also interesting to observe that in all nine K18 models R2 contains the highest β-structure population ranging from 39.3% for K18-3 to 61.0% for K18-8. Similarly, in six of nine K18 models, R4 contains a higher percentage of β-structure (from 26.2% for K18-5 to 60.3% for K18-8) than R3 (from 23.1% for K18-5 to 30.0% for K18-8). The C terminus of R4 in K18-3, K18-4, and K18-6 adopted random coil structure, consistent with the large RMSDs of the structures. Similar to K18 octamers, R4 in all K19 models had higher β-structure content (from 32.6% for K19-6 to 68.7% for K19-9) than R3 (from 23.1% for K19-3 to 53.8% for K19-9). We can also visualize from Fig. 1 that the limited β-structures in R3 for K18 and K19 octamers mainly locate at the N-terminal ^{306}VQIVYKPVDL^{315} region of R3. Similar to R3, the β-structure-enriched regions in R2 and R4 locate at the beginning sequences of ^{275}VQIINKKLDL^{284} for R2 and ^{337}VEVKSEKLD^{345} for R4. Furthermore, a moderate amount of β-structure appeared at ^{258}SKIGSTENLKH^{268}, which was the C-terminal strand of R1 right before the flexible PGGG segment. Different β-structure locations in different models indicate that not only the known paired helical filament segments at the beginning of R2 and R3 but also the end of R1 and the beginning of R4 are involved in the formation of the Tau fibrillar core.

The residue-based root mean square fluctuations (RMSFs) are used to measure the motion of each individual residue. The RMSF is projected onto the octamer structures using a blue-white-red scale, in which the stable structural region (RMSF < 3 Å) is colored red, whereas the flexible region (RMSF > 6 Å) is colored blue. The flexible turn region of PGGG that connects two neighboring repeats is colored yellow to separate the individual repeats. It can be seen in Fig. 1 and supplemental Fig. S4 that for most K18 and K19 octamers, the β-sheet structures located at C-terminal strands of R1 and R2 and the N-terminal strands of R3 displayed very small motion with good, compact packing. Despite an overall structural heterogeneity, R1-R2, R1-R3, and R2-R3 interfaces were well organized by these compact and rigid β-structures. The interfaces consisting of β-sheet structure were mainly stabilized by electrostatic interactions, not hydrophobic interactions or hydrogen bonding, and they are likely to serve as the structural core of K18 and K19 for fibril growth via peptide addition along the fibril axis.

TABLE 1
Structural details of different K18 and K19 octamers
RMSD, radius of gyration (Rg), and energy data are averaged from the last 5-ns simulations.

Models	R3 shape	RMSD/Rg	Energy	Population
		Å	*kcal/mol*	*%*
K18-1	U shape	7.0/31.4	−24,137 ± 81	2.79
K18-2	U shape	7.4/37.2	−24,411 ± 65	12.65
K18-3	U shape	8.4/32.6	−24,136 ± 63	2.76
K18-4	U shape	9.9/34.6	−24,497 ± 165	17.28
K18-5	U shape	10.1/36.2	−24,248 ± 70	6.15
K18-6	U shape	10.0/34.3	−24,370 ± 57	10.48
K18-7	L shape	6.4/32.2	−24,475 ± 57	16.08
K18-8	L shape	5.8/31.6	−24,403 ± 67	12.28
K18-9	Straight	6.2/35.7	−24,697 ± 98	19.53
K19-1	U shape	6.2/28.3	−18,914 ± 58	16.63
K19-2	U shape	6.8/31.8	−18,971 ± 56	19.37
K19-3	U shape	7.4/30.9	−18,726 ± 55	6.18
K19-4	L shape	6.4/31.6	−18,884 ± 57	14.98
K19-5	L shape	6.0/31.3	−18,759 ± 59	7.95
K19-6	U shape	10.6/32.2	−18,526 ± 51	1.33
K19-7	U shape	13.3/30.9	−18,732 ± 50	6.34
K19-8	L shape	4.1/28.6	−18,799 ± 49	10.27
K19-9	Straight	5.7/34.1	−18,923 ± 97	16.93

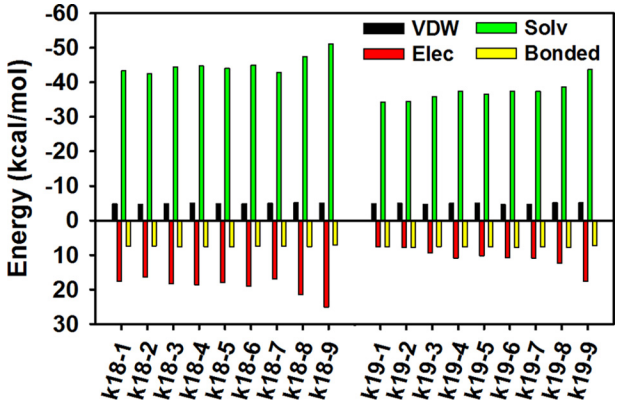

FIGURE 3. **Interaction energies of all K18 and K19 octamers including van der Waals (*VDW*), electrostatic (*Elec*), bonded, and solvation (*Solv*) terms, calculated by the GBMV method.** All K18 and K19 octamers display similar interaction distributions, although they possess significant diversity in structural organization and dynamics.

Heterogeneous Structures Suggest Polymorphic Nature of K18 and K19 Oligomers—Because of the complex kinetics of amyloid formation, nine K18 and nine K19 octamers are likely to represent only a very small percentage of the conformational sampling space. Nevertheless, the carefully selected models can cover the most representative organizations. The averaged conformation energies of K18/K19 octamers over the last 5 ns were calculated using the GBMV (Table 1). To more precisely estimate the overall structural populations for each K18/K19 octamer rather than direct comparison of averaged conformational energies for all models, we extracted a total of 11250 structures from different MD trajectories to compute the structural probability of each model using an in-house Monte Carlo method.

Among nine K18 octamers, the top four energetically favorable models were K18-9 (19.53%, SL shape), K18-4 (17.28%, U shape), K18-7 (16.08%, L shape), and K18-2 (12.65%, U shape). Three U-shaped K18 octamers of K18-1, K18-3, and K18-5 had rather lower structural populations of 2.79, 2.76, and 6.15%, respectively. K18-8 (12.28%, ranking fifth) displayed the best structural integrity but did not present the highest structural population. This suggests that explicit solvent effect should be fully considered in estimating the structural populations. For K19 octamers, the top four octamers with the highest populations were K19-2 (19.37%, U shape), K19-9 (16.93%, SL shape), K19-1 (16.63%, U shape), and K19-4 (14.98%, L shape). Removal of R2 from the R1/R2/R3/R4 sequence made the folding of the peptide into a U-shape conformation energetically more favorable. K19-2 (ranking first), K19-9 (ranking second), K19-1 (ranking third), and K19-4 (ranking fourth) without R2 structurally corresponded to K18-2 (ranking fourth), K18-9 (ranking first), K18-1 (ranking eighth), and K18-7 (ranking third) with R2. K19-8 (10.27%) had the same ranking of fifth as K18-8 among the K18 octamers. Similar structural arrangements of Tau, with stable and low energy conformations between the K18 and K19 models, can provide the structural foundation for the growing K18 (K19) peptides on the K19 (K18) templates (*i.e.* cross-seeding). Based on structural stability and population analysis, K18-2/K19-2 and K18-9/K19-9 are very likely to grow fibrils via cross-seeding because they share large structural overlaps between templated seeds and added peptides.

K18 and K19 Have Different Core Repeats for Conformational Selection—Comparison among various K18 and K19 octamers reveals different dynamical behavior, strongly depending on the conformation of R1, R2, R3, and R4 repeats and interfacial interactions between two neighboring repeats. Conformational energy profiles averaged by residue number for each octamer were given in Fig. 3. Surprisingly, all octamer models shared similar distributions of the different energy terms, although they possessed a significant structural diversity in terms of overall structure and secondary structure. In all cases, van der Waals energy ranging from −4.72 to −5.22 kcal/mol per residue provided small but favorable peptide-peptide interactions to retain peptide association, whereas large electrostatic repulsion (16.37–25.12 kcal/mol per residue for K18 octamers and 7.68–17.60 kcal/mol per residue for K19 octamers) tended to disfavor the compact side chain packing near the interfaces of octamers. To compensate for unfavorable electrostatic interactions, large solvent-accessible surface areas of charged residues and salt bridges contributed the most favorable solvation energy of (−42.50 to −51.03 kcal/mol per residue for K18 octamers and −34.33 to −43.69 kcal/mol per residue for K19 octamers) to alleviate the electrostatic repulsion. Solvent effect clearly plays a pronounced role in stabilizing the Tau isoforms.

Although the per residue total energy for all K18 and K19 octamers was maintained at −23.59 ± 0.23 kcal/mol, it is clear that the exclusion of R2 in K19 octamers increases electrostatic repulsion and decreases their solvation energies, implying that the conformational difference between K18 and K19 octamers leads to potential differences in sensitivity to environmental factors such as pH, ionic strength, and heparin concentrations. Residue-based solvent-accessible surface area for each repeat in K18 and K19 octamers is also measured (Fig. 4). Removing R2 from K18 octamers, residue-based solvent-accessible surface area of R1 and R4 in nine K18 octamers decreased from 54.03 to 49.57 $Å^2$ and from 59.54 to 58.35 $Å^2$, and R3 increased from 40.87 to 42.63 $Å^2$ for K19 octamers. In conclusion, the R2 repeats in the K18 octamer have three effects: 1) increase of solvent-accessible surface area of K18; 2) interaction between

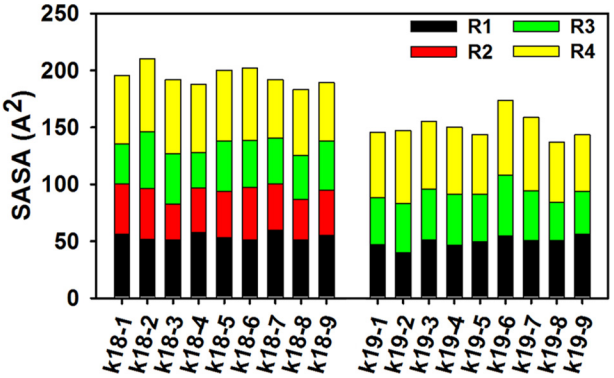

FIGURE 4. **Averaged solvent-accessible surface area of R1, R2, R3, and R4 repeats in K18 and K19 octamers.**

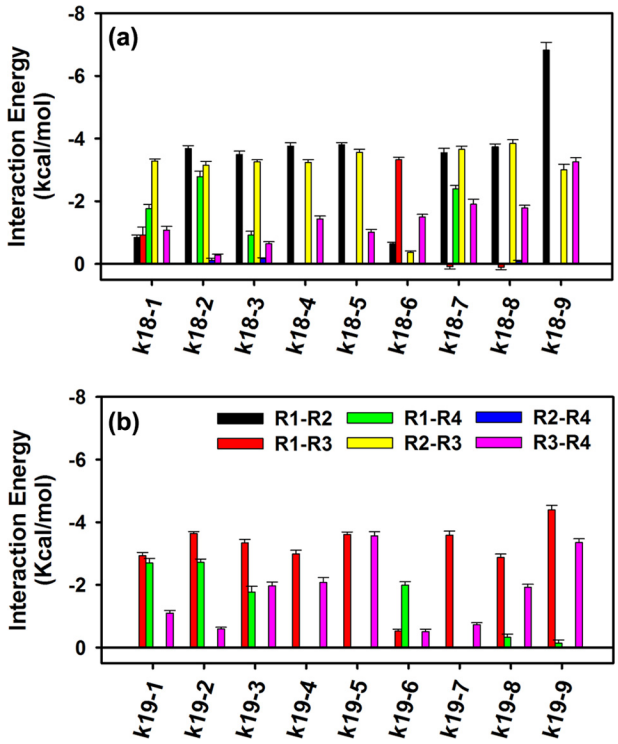

FIGURE 5. **Interaction energies between two neighboring repeats in K18 octamers (*a*) and K19 octamers (*b*).**

R1-R2 and R2-R3 decreased the probability of formation of an R1-R3 interface in K18 aggregates (K18-6 ranks sixth in population); and 3) indirect disturbance of the structure of R4 repeats.

The stable structural regions with significant β-sheet structure are illustrated in Fig. 1. These regions are located mainly at the interfaces. Therefore, the residue-based interaction energy is calculated between two repeats of K18 and K19 models (Fig. 5). Further energy decomposition shows that electrostatic interaction energy contributed more than 90% of the favorable interactions in all K18 and K19 models, suggesting that electrostatic interaction is the dominant adhesive force to preserve the stable regions inside K18 and K19 octamers. For K18 octamers, R1-R2 (−3.49 to −6.82 kcal/mol per residue with exclusion of K18-1) or R2-R3 (−3.00 to −3.84 kcal/mol per residue with exclusion of K18-6) interfaces showed the strongest favorable interactions. The R1-R2 interaction energy was nearly twice as large as other K18 octamers, contributed by two pairs of salt bridges of Asp^{252}–Lys^{290} and Glu^{264}–Lys^{280} in each peptide chain and by the optimized side chain arrangement at the R1-R2 interface in K18-9. Without the R2 building block, the R1-R3 and R3-R4 interaction energies in K19 octamers were improved as compared with K18 octamers. The averaged R3-R4 residue-based interaction energy of K19 octamers (−1.76 kcal/mol per residue) was 0.33 kcal/mol lower than that of K18 octamers (−1.43 kcal/mol per residue). Strong R3-R4 interactions preserve more β-sheet structure (45.06% averaged from nine models) in K19 octamers than in K18 octamers (33.49% averaged from nine models). Therefore, the electrostatic force drives the folding and association of Tau repeats for both space search and energetic optimization preference, implying the importance of the charged/hydrophilic residue arrangement at the repeat-repeat interface and the role of heparin in Tau peptide aggregation.

The above analysis demonstrated that K18 and K19 have different core units in amyloid growth. It is obvious that R2 is the most important repeat in most K18 structures, providing structural and energetic stability. A similar role is observed for R3 in the K19 structures. Thus, in amyloid growth, R2 in K18 and R3 in K19 are expected to act as the primary template for conformational selection, locking and stabilizing incoming monomers into overall fibril structure.

Further secondary structure calculation of K18 octamers in supplemental Fig. S4 and RMSF projection in Fig. 1 have shown that R2 is a stable region in K18 with higher β-structure population than the R3 and R4 repeats. As illustrated in Fig. 6, R2 is the most stable repeat in K18 and acts as structural core in K18 fibrils. It is the most important conformation selection template to catalyze K18 amyloid growth. However, when R2 is excluded in K19, we found out that β-structure population of R3 in K19 increased by more than 4% as compared with R3 in K18. The different conformational selection units may delay the K18 seeded fibril growth of K19. However, when using K19 seed to catalyze the K18 fibril formation, both K18 and K19 have the R3 repeat, and $R3_{K18}$-$R3_{K19}$ recognition prevents such a delay.

K18/K19 Cross-seeding Can Magnify Structural Polymorphism—The recent cross-seeding experiments by Dinkel *et al.* (4) showed an asymmetric structural barrier between K18 and K19 fibrillar aggregates, but no detailed structural information is available to further illustrate the potential mechanism of cross-seeding between K18 and K19 aggregates. We suggest that the feasibility of cross-seeding between different fibrils should be a compromise of both structural similarity and structural population in solution.

In principle, the dominant conformation to allow the cross-seeding between 4R and 3R Tau proteins should come from regions with sequence and the structural identity, which can lead to the exact matches between R1, R3, and R4 regions in K18 (4R) and K19 (3R). The conformation pair that satisfies this requirement is K18-6 and K19-7 (Fig. 7*a*). The R2 repeat in the K18-6 conformation is extruded from the main core of R1-R3-R4, which could have an exact match in K19-7. However, our results revealed that both K18-6 and K19-7 are minor popula-

tions for K18 (10%) and K19 (6%). Thus, cross-seeding between K18 and K19 could be mainly contributed from other conformations.

To check the possibility of cross-seeding using other conformations, we selected R3 for superimposing K18 and corresponding K19 octamers. Five additional structures with the highest structural match (K18-2/K19-2, K18-3/K19-3, K18-7/K19-4, K18-8/K19-8, and K18-9/K19-9) were found to have a potential for cross-seeding (Fig. 7). However, the small population of K18-3 and the poor conformational match between R2 in K18-3 and R1 in K19-3 may decrease the chance for successful cross-seeding with conformations K18-3/K19-3. The small population of K19-7 and the large population difference may decrease the chance for successful cross-seeding with conformations K18-6/K19-7. The other four pairs of candidates, K18-2/K19-2, K18-7/K19-4, K18-8/K19-8, and K18-9/K19-9, satisfied all the prerequisites for cross-seeding: high structural similarity, high population, and small population difference. Even though cross-seeding with conformations selected from these four pairs faces a potential sequence barrier—repeat R1 in K19 has to interact with repeat R2 in K18—the high sequence similarity among the repeats suggests that an interaction between the R1 in K19 and R2 in K18 is likely to happen.

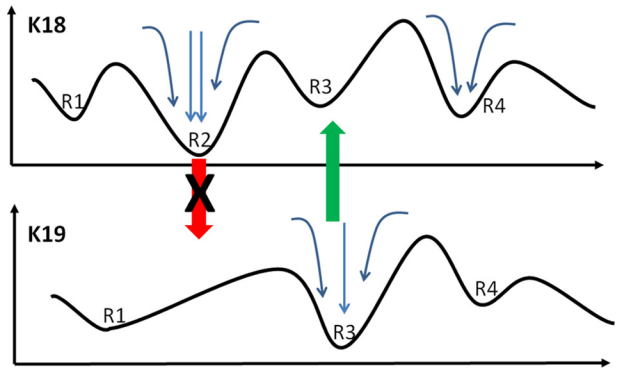

FIGURE 6. **Illustration of the free energy landscape of K18 and K19 and the cross-seeding barrier between K18 and K19 fibrils.** K18 (*top panel*) has four repeats and the most stable one is R2, which may have the highest structure population and forms the core of the K18 fibril. K19 (*bottom panel*) has three repeats and the core repeat is R3, which has the highest structure population. When K18 acts as seeds, the R2 is the catalytic center, and the R2 should recruit the similar peptide with similar conformation into growing fibril. Because the R2 repeat is missing in K19, the barrier exists for K18 seeded K19 growth. When using K19 as seed, the R3 is the catalytic center for conformational selection. R3 in K19 is able to recruit R3 in K18.

Thus, our structural and population studies of K18 and K19 imply that cross-seeding between K18 and K19 would magnify the structural polymorphism of K18 and K19. For five of the six structural pairs examined in this work, K18 presents a more heterogeneous landscape than the corresponding K19. At first sight, it seems that K18 might be able to seed the amyloid formation of K19 easily. In reality, the higher structural polymorphism resulting from K18 as seed may impede its ability to provide effective templates for fast fibril growth, because its diverged structural forms would decrease the formation of the leading fibril form. Fluorescence experiments indicated that K19 might stay in solution because no shift in the fluorescence emission for K19 in the presence of K18 seeds was observed (4). These data are further supported by our sedimentation experiments, which revealed that K19 grows onto K19 seeds but not onto K18 seeds (Fig. 8). Structural polymorphism of K18 may greatly reduce the concentration of seeds that are actually competent to recruit K19.

DISCUSSION

Two types of Tau isoforms, K18 and K19 octamers with different structural symmetries, are computationally modeled by parallel alignment of eight K18/K19 peptides into U-, L-, and SL-shaped structures, followed by explicit solvent MD simulations to assess their structures, dynamics, and populations. All of the isoforms tend to develop into different polymorphic structures with different populations. The stable structures display a compromise of the balance of electrostatic interactions and solvation, and salt bridges formed within the repeat-repeat interfaces and at the peptide terminals play a dominant role in structural stabilization. Our models are in agreement with experimental observation in size, β-structure distribution, and the solvent accessibility of each repeat in the Tau isoforms.

The deposition of amyloid-like filaments in the brain is the central event in the pathogenesis of neurodegenerative disease. Similar to other amyloidgenic peptides, Tau isoforms are highly polymorphic and can aggregate into different ribbon-like fibrils with varied structure and stability (15). Experimentation has already provided evidence that the aggregation of Tau protein or the fragment K18/K19 is a nucleation-dependent and protein-specific polymerization process (26, 42). Understanding the fibrillization-related Tau oligomer structure holds promise as a therapeutic target for neurodegeneration. 4R or 3R Tau (K18 or K19) isoforms are thought to form the core of Tau

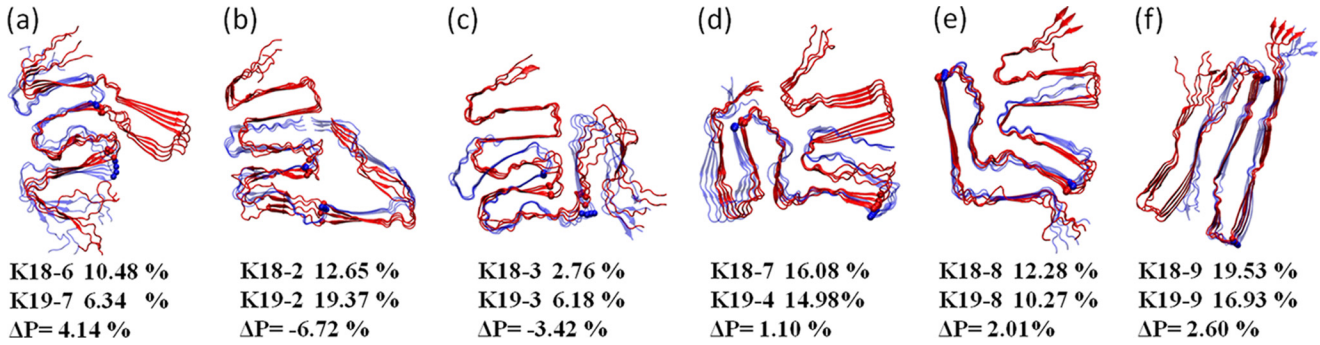

FIGURE 7. **Superimposition of R3 on K18-6/K19-7 (*a*), K18-2/K19-2 (*b*), K18-3/K19-3 (*c*), K18-7/K19-7 (*d*), K18-8/K19-8 (*e*), and K18-9/K19-9 (*f*).** K18 octamers are colored *blue*, and K19 octamers are colored *red*. The C_α atoms of N-terminal residue Val^{306} and C-terminal residue Gln^{336} of repeat R3 in each model are represented by *blue balls* for K18 and *red balls* for K19. For clarity, only tetramers in the middle part of the models are rendered with cartoon mode.

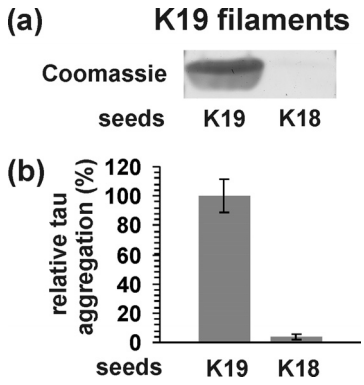

FIGURE 8. **Seeding barrier between K18 and K19.** 10 μM K19 monomers were incubated for 3 h in the presence of 3% K19 seeds or 3% K18 seeds. The samples were sedimented by ultracentrifugation. Pellets were analyzed by 15% SDS-PAGE (*a*) and quantified by densitometry (*b*). All of the values represent the means ± S.D. (n = 3 experiments).

fibrillar structures, but little is known about the molecular structure of K18/K19 oligomers and their relation to amyloid fibril formation and amyloid neurotoxicity. Our computational results provide insights into the structural characterization of K18/K19 octamers by providing energy comparable U, L, and SL shape-based structures.

Previous experiments provided valuable structural information on K18/K19 aggregates. Mukrasch *et al.* (19) summarized the secondary structure distribution of K18 based on NMR experiments. C_α signal shifts in K18 residues helped to determine that the ^{275}VQIINKKLDL^{284} and ^{294}KDNIK^{298} in R2, ^{306}VQIVYKPVDL^{314} in R3, and ^{337}VEVKSEKLD^{345} and ^{357}LDNITJV^{361} in R4 are with β-structure, whereas ^{285}SN286, 316SK^{317} and PGGG in each repeat are in a turn conformation in soluble Tau. The averaged β-structure probability of our nine K18 octamer models (supplemental Fig. S4 in supplementary material) confirms the observation of Mukrasch *et al.* Our calculation also indicates more β-enriched regions in all of the four repeats of K18 octamers. The stable regions of K18 and K19 octamers are measured from the final averaged structures (supplemental Table S1). The dimensions of models with high populations are consistent with experimental measurements based on AFM images (15), which indicate that the heights of K18 fibrils are ~8.0 ± 1.4 or 8.8 ± 1.0 nm, and those of K19 fibrils are 6.9 ± 0.8 or 10.2 ± 1.2 nm.

Unlike the amyloid growth by short peptides, only a small core portion out of the long protein sequence controls the overall conformational selection in amyloid growth. Here, we demonstrated that formation of stable R2 and R3 conformations is the critical step for K18 aggregation and that R3 should be critical for K19 fibril formation. The different core units in K18 and K19 may create cross-seeding barrier for K18 to trigger K19 fibril growth, because R2 is not available in K19.

Even though the amyloid landscape is highly polymorphic and our current simulations cannot afford to explore all structural possibilities, our K18/K19 simulations provided insights into cross-seeding involving heterogeneous structures. The polymorphic nature of protein aggregation could be magnified in the cross-seeding process, which could impede the fibril formation. Such effect could also contribute to the asymmetric barrier between K18 and K19. The higher exposed charge in R2 in K18 than in R3 in K18/K19 (supplemental Fig. S5) is reminiscent of the role of polyanions in nucleating Tau isoforms, *i.e.* polyanions can shift the free energy landscape to promote the formation of dominant conformations.

Acknowledgments—The simulations had been performed using the high performance computational facilities of the Biowulf PC/Linux cluster at the National Institutes of Health.

REFERENCES

1. Hardy, J., and Allsop, D. (1991) Amyloid deposition as the central event in the aetiology of Alzheimer's disease. *Trends Pharmacol. Sci.* **12,** 383–388
2. Hardy, J. A., and Higgins, G. A. (1992) Alzheimer's disease. The amyloid cascade hypothesis. *Science* **256,** 184–185
3. Drubin, D. G., and Kirschner, M. W. (1986) Tau protein function in living cells. *J. Cell Biol.* **103,** 2739–2746
4. Dinkel, P. D., Siddiqua, A., Huynh, H., Shah, M., and Margittai, M. (2011) Variations in filament conformation dictate seeding barrier between three- and four-repeat Tau. *Biochemistry* **50,** 4330–4336
5. Goedert, M., Spillantini, M. G., Jakes, R., Rutherford, D., and Crowther, R. A. (1989) Multiple isoforms of human microtubule-associated protein Tau. Sequences and localization in neurofibrillary tangles of Alzheimer's disease. *Neuron* **3,** 519–526
6. Goedert, M., Spillantini, M. G., Cairns, N. J., and Crowther, R. A. (1992) Tau proteins of Alzheimer paired helical filaments. Abnormal phosphorylation of all six brain isoforms. *Neuron* **8,** 159–168
7. Schweers, O., Schönbrunn-Hanebeck, E., Marx, A., and Mandelkow, E. (1994) Structural studies of Tau protein and Alzheimer paired helical filaments show no evidence for β-structure. *J. Biol. Chem.* **269,** 24290–24297
8. Cleveland, D. W., Hwo, S. Y., and Kirschner, M. W. (1977) Physical and chemical properties of purified Tau factor and the role of Tau in microtubule assembly. *J. Mol. Biol.* **116,** 227–247
9. Berriman, J., Serpell, L. C., Oberg, K. A., Fink, A. L., Goedert, M., and Crowther, R. A. (2003) Tau filaments from human brain and from in vitro assembly of recombinant protein show cross-β structure. *Proc. Natl. Acad. Sci. U.S.A.* **100,** 9034–9038
10. von Bergen, M., Barghorn, S., Li, L., Marx, A., Biernat, J., Mandelkow, E. M., and Mandelkow, E. (2001) Mutations of Tau protein in frontotemporal dementia promote aggregation of paired helical filaments by enhancing local β-structure. *J. Biol. Chem.* **276,** 48165–48174
11. Congdon, E. E., Kim, S., Bonchak, J., Songrug, T., Matzavinos, A., and Kuret, J. (2008) Nucleation-dependent Tau filament formation. The importance of dimerization and an estimation of elementary rate constants. *J. Biol. Chem.* **283,** 13806–13816
12. Xu, S. H., Brunden, K. R., Trojanowski, J. Q., and Lee, V. M., (2010) Characterization of Tau fibrillization *in vitro*. *Alzheimers Dement.* **6,** 110–117
13. Wischik, C. M., Novak, M., Thøgersen, H. C., Edwards, P. C., Runswick, M. J., Jakes, R., Walker, J. E., Milstein, C., Roth, M., and Klug, A. (1988) Isolation of a fragment of Tau derived from the core of the paired helical filament of Alzheimer disease. *Proc. Natl. Acad. Sci. U.S.A.* **85,** 4506–4510
14. von Bergen, M., Barghorn, S., Müller, S. A., Pickhardt, M., Biernat, J., Mandelkow, E. M., Davies, P., Aebi, U., and Mandelkow, E. (2006) The core of Tau-paired helical filaments studied by scanning transmission electron microscopy and limited proteolysis. *Biochemistry* **45,** 6446–6457
15. Wegmann, S., Jung, Y. J., Chinnathambi, S., Mandelkow, E. M., Mandelkow, E., and Muller, D. J. (2010) Human Tau isoforms assemble into ribbon-like fibrils that display polymorphic structure and stability. *J. Biol. Chem.* **285,** 27302–27313
16. Li, L., von Bergen, M., Mandelkow, E. M., and Mandelkow, E. (2002) Structure, stability, and aggregation of paired helical filaments from Tau protein and FTDP-17 mutants probed by tryptophan scanning mutagenesis. *J. Biol. Chem.* **277,** 41390–41400
17. Mukrasch, M. D., von Bergen, M., Biernat, J., Fischer, D., Griesinger, C., Mandelkow, E., and Zweckstetter, M. (2007) The "jaws" of the Tau-micro-

tubule interaction. *J. Biol. Chem.* **282,** 12230–12239
18. Margittai, M., and Langen, R. (2004) Template-assisted filament growth by parallel stacking of Tau. *Proc. Natl. Acad. Sci. U.S.A.* **101,** 10278–10283
19. Mukrasch, M. D., Biernat, J., von Bergen, M., Griesinger, C., Mandelkow, E., and Zweckstetter, M. (2005) Sites of Tau important for aggregation populate β-structure and bind to microtubules and polyanions. *J. Biol. Chem.* **280,** 24978–24986
20. Siddiqua, A., and Margittai, M. (2010) Three- and four-repeat Tau coassemble into heterogeneous filaments. An implication for Alzheimer disease. *J. Biol. Chem.* **285,** 37920–37926
21. Csermely, P., Palotai, R., and Nussinov, R. (2010) Induced fit, conformational selection and independent dynamic segments. An extended view of binding events. *Trends Biochem. Sci.* **35,** 539–546
22. Ma, B., Kumar, S., Tsai, C. J., and Nussinov, R. (1999) Folding funnels and binding mechanisms. *Protein Eng.* **12,** 713–720
23. Ma, B., and Nussinov, R. (2010) Enzyme dynamics point to stepwise conformational selection in catalysis. *Curr. Opin. Chem. Biol.* **14,** 652–659
24. Ma, B., and Nussinov, R. (2012) Selective molecular recognition in amyloid growth and transmission and cross-species barriers. *J. Mol. Biol.*, in press
25. Frost, B., and Diamond, M. I. (2010) Prion-like mechanisms in neurodegenerative diseases. *Nat. Rev. Neurosci.* **11,** 155–159
26. Frost, B., Jacks, R. L., and Diamond, M. I. (2009) Propagation of Tau misfolding from the outside to the inside of a cell. *J. Biol. Chem.* **284,** 12845–12852
27. Clavaguera, F., Bolmont, T., Crowther, R. A., Abramowski, D., Frank, S., Probst, A., Fraser, G., Stalder, A. K., Beibel, M., Staufenbiel, M., Jucker, M., Goedert, M., and Tolnay, M. (2009) Transmission and spreading of tauopathy in transgenic mouse brain. *Nat. Cell Biol.* **11,** 909–913
28. Miller, Y., Ma, B., and Nussinov, R. (2011) Synergistic interactions between repeats in Tau protein and Aβ amyloids may be responsible for accelerated aggregation via polymorphic states. *Biochemistry* **50,** 5172–5181
29. Ma, B., and Nussinov, R. (2002) Stabilities and conformations of Alzheimer's β-amyloid peptide oligomers (Aβ 16–22, Aβ 16–35, and Aβ 10–35). Sequence effects. *Proc. Natl. Acad. Sci. U.S.A.* **99,** 14126–14131
30. Zheng, J., Ma, B., and Nussinov, R. (2006) Consensus features in amyloid fibrils. Sheet-sheet recognition via a (polar or nonpolar) zipper structure. *Phys. Biol.* **3,** P1–4
31. Miller, Y., Ma, B., and Nussinov, R. (2010) Polymorphism in Alzheimer Aβ amyloid organization reflects conformational selection in a rugged energy landscape. *Chem. Rev.* **110,** 4820–4838
32. Ma, B., and Nussinov, R. (2011) Polymorphic triple β-sheet structures contribute to amide hydrogen/deuterium (H/D) exchange protection in the Alzheimer amyloid β42 peptide. *J. Biol. Chem.* **286,** 34244–34253
33. Ma, B., and Nussinov, R. (2010) Polymorphic C-terminal β-sheet interactions determine the formation of fibril or amyloid beta-derived diffusible ligand-like globulomer for the Alzheimer Aβ42 dodecamer. *J. Biol. Chem.* **285,** 37102–37110
34. Kale, L., Skeel, R., Bhandarkar, M., Brunner, R., Gursoy, A., Krawetz, N., Phillips, J., Shinozaki, A., Varadarajan, K., and Schulten, K. (1999) NAMD2: greater scalability for parallel molecular dynamics. *J. Comput. Phys.* **151,** 283–312
35. Mackerell, A. D., Jr., Feig, M., and Brooks, C. L., 3rd (2004) Extending the treatment of backbone energetics in protein force fields. Limitations of gas-phase quantum mechanics in reproducing protein conformational distributions in molecular dynamics simulations. *J. Comput. Chem.* **25,** 1400–1415
36. Lee, M. S., Salsbury, F. R., and Brooks, C. L. (2002) Novel generalized Born methods. *J. Chem. Phys.* **116,** 10606–10614
37. Zheng, J., Ma, B., Chang, Y., and Nussinov, R. (2008) Molecular dynamics simulations of Alzheimer Aβ40 elongation and lateral association. *Front. Biosci.* **13,** 3919–3930
38. Sibille, N., Sillen, A., Leroy, A., Wieruszeski, J. M., Mulloy, B., Landrieu, I., and Lippens, G. (2006) Structural impact of heparin binding to full-length Tau as studied by NMR spectroscopy. *Biochemistry* **45,** 12560–12572
39. Frishman, D., and Argos, P. (1995) Knowledge-based protein secondary structure assignment. *Proteins* **23,** 566–579
40. Cerf, E., Sarroukh, R., Tamamizu-Kato, S., Breydo, L., Derclaye, S., Dufrêne, Y. F., Narayanaswami, V., Goormaghtigh, E., Ruysschaert, J. M., and Raussens, V. (2009) Antiparallel β-sheet. A signature structure of the oligomeric amyloid β-peptide. *Biochem. J.* **421,** 415–423
41. Matsumura, S., Shinoda, K., Yamada, M., Yokojima, S., Inoue, M., Ohnishi, T., Shimada, T., Kikuchi, K., Masui, D., Hashimoto, S., Sato, M., Ito, A., Akioka, M., Takagi, S., Nakamura, Y., Nemoto, K., Hasegawa, Y., Takamoto, H., Inoue, H., Nakamura, S., Nabeshima, Y., Teplow, D. B., Kinjo, M., and Hoshi, M. (2011) Two distinct amyloid β-protein (Aβ) assembly pathways leading to oligomers and fibrils identified by combined fluorescence correlation spectroscopy, morphology, and toxicity analyses. *J. Biol. Chem.* **286,** 11555–11562
42. Nonaka, T., Watanabe, S. T., Iwatsubo, T., and Hasegawa, M. (2010) Seeded aggregation and toxicity of α-synuclein and Tau. Cellular models of neurodegenerative diseases. *J. Biol. Chem.* **285,** 34885–34898